

Electron-phonon driven charge density wave and superconductivity in a 1T-TaSi₂N₄ monolayerLuo Yan ^{1,2}, Ruiqi Ku,³ Jian-Guo Si ¹, Peng-Fei Liu ^{1,4}, Hao Gao ^{5,*}, Liujiang Zhou ^{2,†} and Bao-Tian Wang ^{1,4,6,‡}¹*Institute of High Energy Physics, Chinese Academy of Science (CAS), Beijing 100049, China*²*School of Physics, University of Electronic Science and Technology of China, Chengdu 610054, China*³*School of Physics, Harbin Institute of Technology, Harbin 150001, China*⁴*Spallation Neutron Source Science Center, Dongguan 523803, China*⁵*Fritz-Haber-Institut der Max-Planck-Gesellschaft, Faradayweg 4-6, 14195 Berlin, Germany*⁶*Collaborative Innovation Center of Extreme Optics, Shanxi University, Taiyuan, Shanxi 030006, China* (Received 18 December 2023; revised 11 March 2024; accepted 13 March 2024; published 1 April 2024)

Charge-density wave (CDW) and superconductivity, as well as their interplay, are fascinating topics in condensed-matter physics. In this work, we propose a single-layer (SL) CDW material, 1T-TaSi₂N₄, among synthesized two-dimensional (2D) MoSi₂N₄ family. Through first-principles simulations, its stability, vibrational properties, electronic structures, CDW, and superconductivity have been systematically scrutinized. The Ta-*d*_{z²} orbitals occupy mainly at the Fermi level and SL 1T-TaSi₂N₄ exhibits intrinsic metallic property. Besides, the CDW transition temperature (T_{CDW}) is estimated to be ~ 500 K by using the temperature dependent effective potential technique. We found that it is the electron-phonon coupling (EPC) that drives the CDW to form. Furthermore, its CDW orders can be manipulated by carrier doping and applying strain. At doping of 0.14 h/cell, the CDW instability is effectively suppressed and it changes to a 2D superconductor below ~ 21.84 K. Moreover, its superconducting transition temperature T_c under the strain of 10% is ~ 10.47 K. Physically, the superconductivity in stabilized 1T-TaSi₂N₄ monolayer is mainly contributed by the EPC between electrons from the Ta-*d*_{z²} orbitals and phonon vibrations from the Ta-*xy* and N-*z* modes with evident soft phonon mode.

DOI: [10.1103/PhysRevB.109.134502](https://doi.org/10.1103/PhysRevB.109.134502)**I. INTRODUCTION**

Charge density wave (CDW) and superconductivity, as the famous collective quantum phenomena, have attracted widespread attention in condensed matter physics [1–4]. However, CDW and superconductivity induced by the electronic instabilities, always having intricate interplay, require being further understood. Fortunately, many two-dimensional (2D) transition-metal dichalcogenides (TMDs) supply proper platforms to investigate the CDW, superconductivity, and their interplay [5–8]. In order to explore the accurate mechanism of CDW in 2D TMDs, some possible strategies have been proposed, such as the Fermi surface (FS) nesting [9,10], strong electron-phonon coupling (EPC) [11,12], and excitonic insulator [3,13,14]. Meanwhile, it has been observed that the incommensurate/nearly commensurate CDW orders in many 2D TMDs can coexist with the superconductivity via the formation of CDW domain walls [15–17]. This character is distinct from CuO₂ monolayer, which exhibits a clear competition between its CDW and superconductivity, by performing scanning tunneling microscope measurements [18]. In this respect, the question of whether CDWs compete or coexist with superconductivity remains elusive. On the other hand, CDW transition temperature (T_{CDW}) near room temperature is

desired for realistic applications [6,8,19,20]. Therefore, more feasible candidates should be raised to explore CDW and superconductivity in 2D materials.

Inspiringly, the MoSi₂N₄ monolayer has been effectively obtained in the centimeter scale using the chemical vapor deposition growth method [21]. This has stimulated the predictions of a large family of such monolayer materials [21,22], which can be regarded as a transition-metal dinitrides (MN₂) monolayer saturated by the Si-N layers on its two sides. Since MN₂ monolayers possess two general phases: 2H trigonal prismatic and 1T octahedral phases, therefore, the MoSi₂N₄ family materials also show structural diversities [22,23]. As a consequence, MoSi₂N₄ family materials possess plentiful physiochemical properties, favoring further applications as photocatalysts [24,25], piezoelectricity materials [26], sensor [27], optics [28], superconductors [22,29], etc. As previously reported [22,29], single-layer (SL) 2H-TaSi₂N₄ is dynamically stable and is a Bardeen-Cooper-Schrieffer (BCS) superconductor, while the 1T phase of TaSi₂N₄ exhibits imaginary phonon frequencies and was neglected. However, for SL 1T-TaSi₂N₄, the locations of the Kohn anomalies at the imaginary acoustic phonon modes generally represent a typical feature of the CDW orders [11,12,30]. Therefore, SL 1T-TaSi₂N₄ would provide an ideal platform to investigate CDW features, superconductivity, and their interplay.

In this work, we determine SL 1T-TaSi₂N₄ as a CDW material, whose CDW orders are originated from the momentum-dependent EPC confirmed by the phonon linewidth distributions. The soft mode, leading to the CDW orders, is mainly

*haogao@fhi-berlin.mpg.de

†liujiang86@gmail.com

‡wangbt@ihp.ac.cn

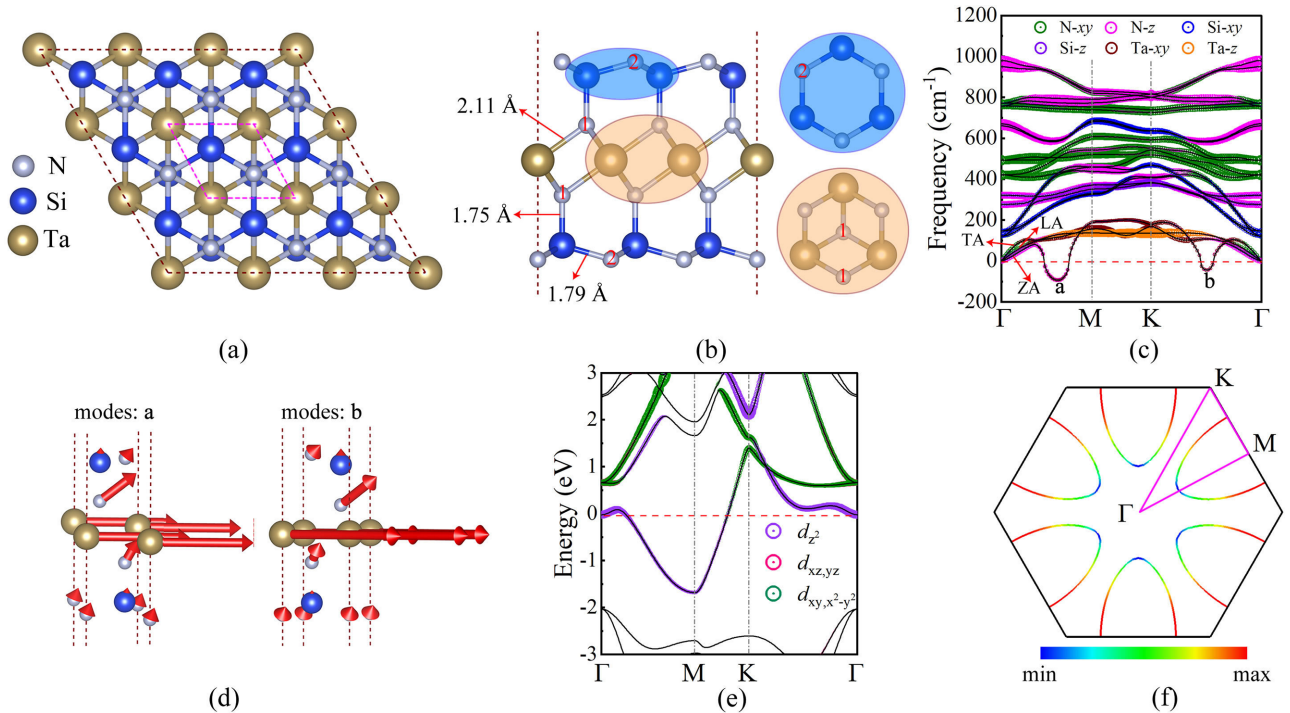


FIG. 1. (a) Top and (b) side views, (c) phonon dispersions, (e) projected band structures, and (f) Fermi surface of SL $1T$ - TaSi_2N_4 . (d) Visualizations of the vibrational modes at **a** and **b** points in (c). The red dashed lines in (a) indicate the primitive cell and the bond lengths are marked in (b). The phonon dispersions are weighted by the motion modes of Ta, Si, and N atoms. The colors drawn in (f) indicate the magnitude of the Fermi velocity. The Fermi level is set to 0 eV.

contributed by the in-plane motions of Ta atoms and the T_{CDW} is estimated to be ~ 500 K based on dynamical simulations. Apart from temperature, CDW orders in metallic $1T$ - TaSi_2N_4 can also be suppressed by doping or strain, leading to the emergence of superconducting states. At the critical doping value of 0.14 h/cell, SL $1T$ - TaSi_2N_4 shows superconducting phase, and its superconducting transition temperature T_c is estimated to be ~ 21.84 K. Besides, when the tensile strain of 10% is applied, it turns to a superconductor with a T_c of ~ 10.47 K, and its T_c can reach to 15.01 K via synchronous doping of 0.3 h/cell.

II. COMPUTATIONAL METHODS

The first-principle calculations were performed by using the QUANTUM ESPRESSO code [31,32] with generalized gradient approximation according to the Perdew-Burke-Ernzerhof functional [33]. The norm-conserving Vanderbilt pseudopotentials [34] were adopted to describe the electron-ion interactions. The total energy and electron charge density were always calculated by Methfessel-Paxton smearing method, except for simulating the electronic temperature with a Fermi-Dirac smearing method. To simulate the monolayer, the vacuum thickness of 15 Å along the z direction was built. After convergence test, the kinetic-energy and charge-density cutoff were set to be 70 and 280 Ry, respectively. The \mathbf{k} -point mesh for self-consistent electron density calculations was set as $36 \times 36 \times 1$. A denser $198 \times 198 \times 1$ \mathbf{k} -point grid was used to calculate the Lindhard function using the measured band structures. The \mathbf{q} -point mesh for phonon properties and EPC simulations was set as $6 \times 6 \times 1$. Since the spin-orbit coupling

(SOC) has little effect on electron and superconductivity of $2H$ - TaSi_2N_4 [29], thus, the SOC was not considered in this work. The *ab initio* molecular dynamics (AIMD) calculations with constant number, volume, temperature (NVT) ensemble were simulated at a series of temperatures using the Nosé-Hoover thermostat, lasting for 10 ps with a time step of 2 fs. Then, the finite-temperature phonon dispersion curves were calculated using the temperature-dependent effective potential (TDEP) method [35,36], as implemented in the Hiphive Package [37], by extracting effective interatomic force constants taking the anharmonicity into account for a given temperature. Here, a $6 \times 6 \times 1$ supercell was adopted. The superconductivity calculations were explored in the framework of BCS theory [38]. Detailed methods were given in the Supplemental Material (SM) [39] (see also Refs. [12,40–43] therein).

III. RESULTS AND DISCUSSIONS

A. Atomic structure for SL $1T$ - TaSi_2N_4

As depicted in Figs. 1(a) and 1(b), SL $1T$ - TaSi_2N_4 can be regarded as a TaN_2 monolayer sandwiched between two Si-N bilayers. Relying on the relative positions of the two N layers within the TaN_2 unit, SL TaSi_2N_4 systems have another octahedral phase different from $2H$ phase [29], namely, $1T$ - TaSi_2N_4 monolayer, in which the two N layers follow the octahedral prismatic coordinations. SL $1T$ - TaSi_2N_4 is a metastable phase and its energy is about 42.86 meV per atom higher than that of the $2H$ phase [29]. In analogy to SL $2H$ - TaSi_2N_4 , SL $1T$ - TaSi_2N_4 also crystallizes in the hexagonal lattice, and has a space group $P3m1$ (No. 157), corresponding to a point symmetry of C_{3v} .

The optimized lattice constants of SL $1T$ -TaSi₂N₄ are $a = b = 2.97$ Å, comparable to those of $2H$ phase (2.96 Å). There are two types of N atoms: N₁ atoms connect the hexagonal Si-N layers with the Ta atoms; N₂ atoms only coordinate with the Si atoms in Si-N₂ layers. According to the electron localization function (see Fig. S1 in SM) [39], the Si-N₁ and Si-N₂ bonds exhibit covalent characters, since the electrons are greatly localized at the center area of the bonds. The Si-N₁ and Si-N₂ bonds are short, only in length of 1.75 and 1.79 Å, respectively. The Ta-N₁ bonds are longer, with a length of 2.11 Å, and show ionic bonding properties due to the highly localized electrons around the N atoms. According to Bader calculations [44], each Si atom denotes 2.21 e and 0.76 e to N₂ and N₁ atoms, respectively, while each Ta atom transfers 0.98 e to N₁ atom. Therefore, the transferring electrons in SL $1T$ -TaSi₂N₄ are about 7.88 e , comparable to those in $2H$ phase (7.78 e), indicating that $1T$ -TaSi₂N₄ could also be a good $2D$ superconductor [29].

B. Thermal, mechanical, and phonon features

The stability of SL $1T$ -TaSi₂N₄ can be explored from thermal, mechanical, and dynamical aspects. By utilizing the AIMD with the Nosé-Hoover thermostat, its thermal stability is estimated at elevated temperatures. To minimize the effects of the periodic boundary conditions, a $4 \times 4 \times 1$ supercell is adopted. The free energy of SL $1T$ -TaSi₂N₄ slightly fluctuates around the equilibrium value during the entire simulation period, and $1T$ -TaSi₂N₄ maintains structural integrity after annealing at 3000 K. However, the crystal shows a huge structural disruption at 3300 K [see Fig. S2(b) in SM] [39]. Therefore, the melting temperature of SL $1T$ -TaSi₂N₄ is evaluated between 3000 and 3300 K, which is higher than that of SL $2H$ -TaSi₂N₄ (2100–2400 K) [29], favoring its fabrications and applications under high temperatures.

The mechanical properties are further assessed by three independent elastic constants (i.e., C_{11} , C_{12} , and C_{66}). The calculated C_{11} , C_{12} , and C_{66} are 487.58, 125.76, and 180.91 N/m, respectively. Clearly, SL $1T$ -TaSi₂N₄ meets the Born criteria, namely, $C_{11}^2 > C_{12}^2$ and $C_{66} > 0$ [45], reflecting its mechanical stability. Based on the calculated C_{ij} values, the orientation-dependent $Y(\theta)$ and $\nu(\theta)$ as a function of the polar angle are shown [see SM Figs. S2(c) and S2(d)] [39]. Clearly, both Y and ν show isotropic characters with perfect circles in the polar diagrams. As a comparison, the orientation-dependent $Y(\theta)$ and $\nu(\theta)$ of SL $2H$ -TaSi₂N₄ are also presented, and $1T$ and $2H$ -TaSi₂N₄ possess nearly identical mechanical features.

The phonon spectrum resolved by atomic vibration modes is shown in Fig. 1(c). At first glance, two obvious Kohn anomalies exhibiting imaginary frequencies distribute along the Γ – M and K – Γ paths, meaning a dynamically unstable nature. However, this behavior is a possible feature for CDW materials, as reported in SL $1T$ -TiSe₂ [20,30], $1T$ -VSe₂ [11], $1T$ -MoSH [12], etc. As indicated in Fig. 1(d), the imaginary modes locating at the **a** and **b** points originate mostly from the in-plane vibrations of the Ta atoms (Ta- xy) with a small contribution from the out-of-plane vibrations of the N₁ atoms (N₁- z). Thus, the soft out-of-plane acoustic (ZA) mode is highly related to the weak ionic bonding between Ta and N₁. Such bonding is possible to be anharmonic and

TABLE I. Summarized the symmetry, vibration, activity, and frequency (cm⁻²) for the 12 optical vibrational modes at the Γ point.

Modes	Symmetry	Vibration	Activity	Frequency
(4, 5)	E	In-plane N ₂ , Si	IR	124.82
(6, 7)	E	In-plane N ₂ , Si	IR	144.41
(8)	A_1	Out-of-plane N ₂ , Si	IR	265.68
(9)	A_1	Out-of-plane N ₂ , Si	IR	320.55
(10, 11)	E	In-plane N ₁	IR	422.62
(12, 13)	E	In-plane N ₁	IR	506.54
(14)	A_1	Out-of-plane N ₁ , Si	IR	653.71
(15)	A_1	Out-of-plane N ₁ , Si	IR	660.15
(16, 17)	E	In-plane N ₂ , Si	IR	755.65
(18, 19)	E	In-plane N ₂ , Si	IR	768.50
(20)	A_1	Out-of-plane N ₁	IR	949.08
(21)	A_1	Out-of-plane N ₁	IR	981.62

may induce the CDW transition upon heating, compressing, or doping. Discussions on CDW will be presented later. Since SL $1T$ -TaSi₂N₄ has seven atoms in its primitive cell, there are 21 phonon modes: 3 acoustic and 18 optical branches. Three acoustic branches are mostly dominated by vibrations of the Ta atoms, constituting the ZA, in-plane transverse acoustic (TA), and in-plane longitudinal acoustic (LA) modes [Fig. 1(c)]. Approaching the Γ point, LA and TA modes show linear dispersions, while ZA mode exhibits a quadratic dependence on the wave vector.

Furthermore, the highest phonon frequency is about 1000 cm⁻², comparable to that of borophene (~ 1100 cm⁻²) [46,47], showing strong covalent bonding interactions within the Si-N layers. To directly reflect the relative motions of Ta, Si, N atoms, the vibration modes at Γ point are visualized (see SM Fig. S3) [39], which are in line with the phonon spectrum in Fig. 1(c). Summarized information about the symmetry, vibration, Raman or infrared activity at Γ point are listed in Table I. At 124.82 and 144.41 cm⁻², the doubly degenerated (4, 5) and (6, 7) modes are dominated by N₂- xy and Si- xy vibrations. At 265.68 and 320.55 cm⁻², the main atomic motions of the (8) and (9) modes are contributed by N₂- z and Si- z vibrations. For the doubly degenerated (10, 11) and (12, 13) modes, the vibration modes are mainly from the N₁- xy vibrations. Besides, the singly degenerated 14th and 15th modes are from N₂- z and Si- z vibrations. For the doubly degenerate (16, 17) modes at 755.65 cm⁻², N₂- xy vibrations in the lower Si-N layer dominate mostly. The N₂- xy vibrations in the upper Si-N layer contribute to the (18, 19) modes. In addition, the singly degenerated 20th and 21th modes are mainly from the N₁- z vibrations.

C. Electron and CDW features

As indicated by the orbital-resolved band structure in Fig. 1(e), SL $1T$ -TaSi₂N₄ is an intrinsic metal with the band crossing the Fermi level. Its metallic features mainly stem from the Ta- d_{z^2} orbitals with visible occupations from the Ta- d_{xy, x^2-y^2} orbitals. There is a separate electronic band near the Fermi level, dividing the Fermi surface (FS) into petal shapes around the Γ point [Fig. 1(f)]. Besides, Fermi velocity is projected on the FS by the color bar, directly relating to the

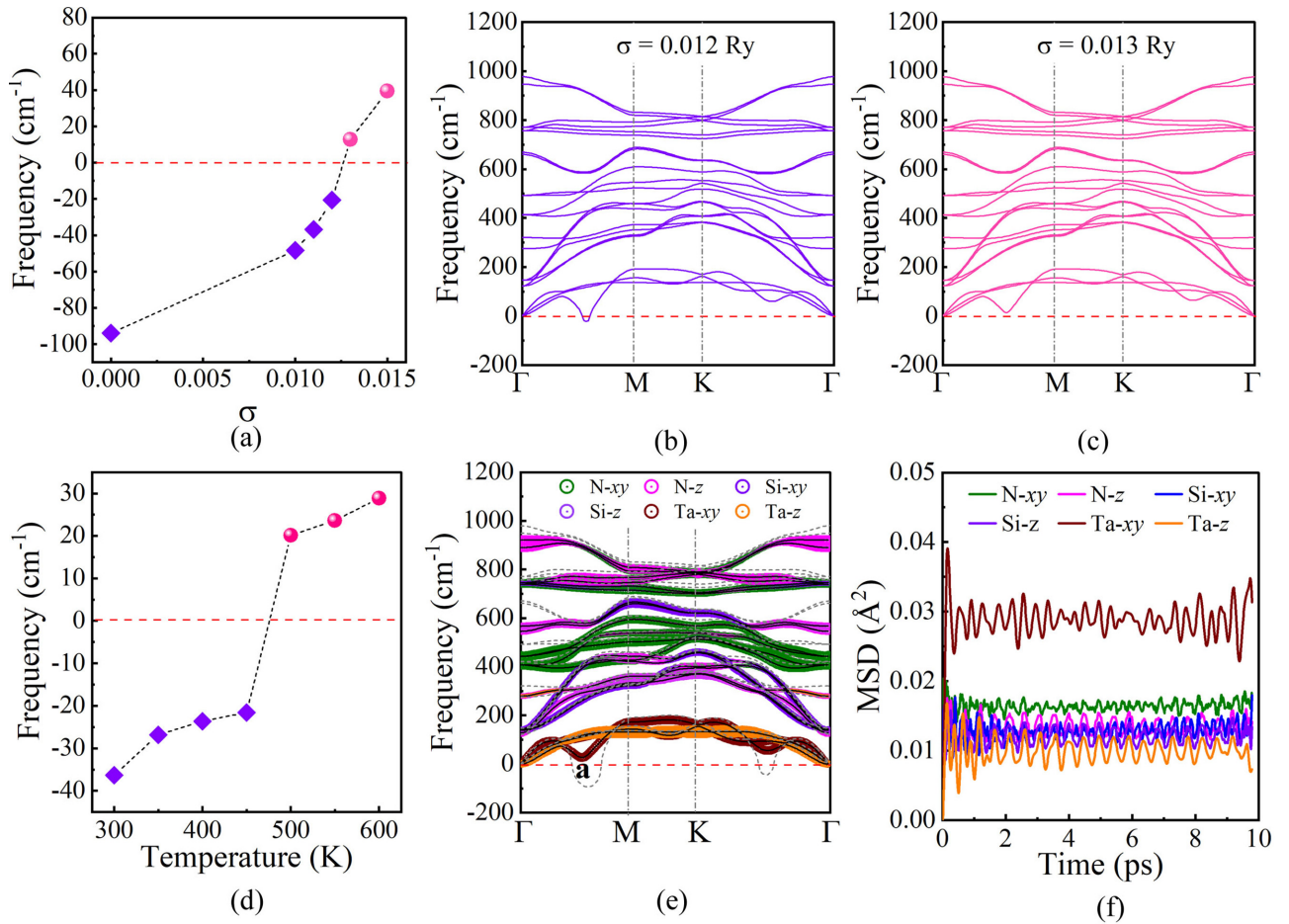


FIG. 2. (a) Phonon frequency of **a** point in Fig. 1(c) along with the increasing σ . Two typical phonon spectra simulated with (b) $\sigma = 0.012$ Ry and (c) $\sigma = 0.013$ Ry. (d) Variations of the frequency of **a** point in Fig. 1(c) along with the increased AIMD temperature from 300 to 600 K. (e) Harmonic (at 0 K) and anharmonic phonon spectra (at AIMD temperature of 500 K) for SL 1T-TaSi₂N₄, calculated on a $6 \times 6 \times 1$ supercell. The gray dotted lines indicate the harmonic phonon spectrum. (f) MSDs of Ta, N and Si atoms obtained from AIMD simulations at 500 K.

slopes of the bands. The high velocity of the FS is along the K–M path, while the velocity along the Γ –M is relatively low. Inspiringly, a flattened band along the K– Γ path locates near the Fermi level, leading to a high density of electron gas just near the Fermi level. In this respect, SL 1T-TaSi₂N₄ may be a good superconductor [48], as already predicted in our previous study of SL 2H-TaSi₂N₄ [29].

As discussed above, SL 1T-TaSi₂N₄ exhibits CDW feature of the Kohn anomalies in its ZA phonon branch. Here, the electronic temperature T_e , which can be directly simulated by the Fermi-Dirac smearing factor σ , is further considered to simulate the T_e dependence of the phonon dispersions [12,20,30,49]. Generally speaking, the suppression of the imaginary phonon frequencies indicates the CDW transition to the normal phase. The variations of the largest imaginary frequency of the **a** point [marked in Fig. 1(c)] along with the increased σ are plotted in Fig. 2(a). By increasing the σ , the imaginary Kohn anomaly at **a** point becomes less evident, and finally can be manipulated to a positive phonon mode using $\sigma = 0.013$ Ry [Figs. 4(b) and 4(c)]. The dependence of the phonon dispersions on σ confirms that the SL 1T-TaSi₂N₄ is a CDW monolayer. It worth noting that the σ is only adopted to simulate CDW features, and cannot represent the

real critical temperature. A more realistic estimation of the T_{CDW} requires methods to treat anharmonicity properly. Here, we conduct the TDEP [50] calculations using the Hiphive package [37] to consider the effects of anharmonicity. Several AIMD simulations are performed under various temperatures (300, 350, 400, 450, 500, 550, and 600 K) and the interatomic force constants are extracted from the AIMD trajectories to obtain the effective phonons under different temperatures. These TDEP simulations are converged as shown in Fig. S4 [39]. The frequencies of the mode **a** depending on the AIMD temperatures are shown in Fig. 2(d). We find that the AIMD temperature can modulate the unstable phonon mode to be stable. As indicated in Fig. 2(e), the frequencies of two soft modes from harmonic approximation become real at 500 K, indicating that SL 1T-TaSi₂N₄ is dynamically stable at temperatures of 500 K and above. From Fig. 2(d), T_{CDW} is roughly around 450–500 K, which is higher than that of 2H-NbSe₂ (100 K) [6] and 1T-TiSe₂ monolayer (230 K) [7] in experiment, and also higher than that of SL 1T-TiSe₂ (440 K) and electron-doped ones (200–280 K) in theory [51]. Here, the similar results of simulated and measured electron-doped SL 1T-TiSe₂ means these methods to evaluate T_{CDW} are reliable. Of course, our simulated results need further experiments to

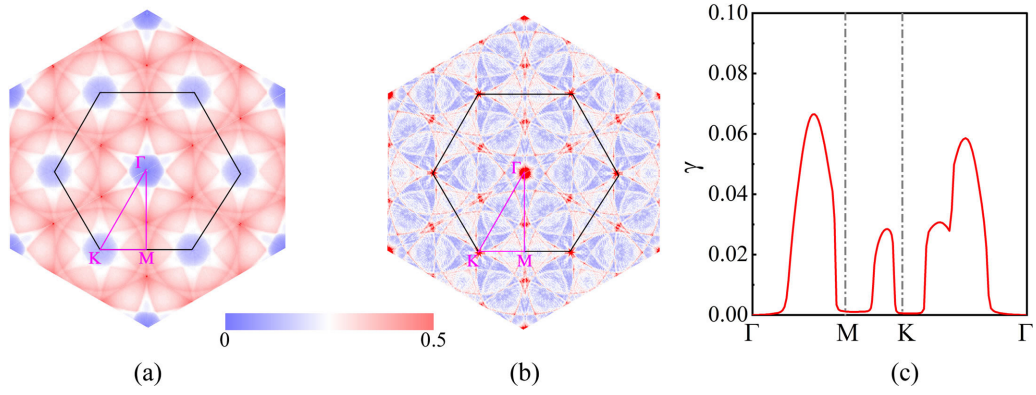


FIG. 3. The real and imaginary parts of electron susceptibility function are plotted in (a) and (b), respectively. (c) The calculated phonon linewidth γ in the ZA branch.

verify. The near room temperature ultrathin CDW materials are desirable for practical applications.

The major soft mode in the anharmonic phonon spectrum [mode **a** in Fig. 2(e)] is dominated by the in-plane mode of Ta atoms, different from the soft mode dominated by

the out-of-plane mode of N atoms in the harmonic phonon spectrum [Fig. 1(c)]. This indicates a significant effect of the anharmonicity, which is further supported by our calculated element-resolved mean square displacements (MSDs) along different directions during MD simulations. As shown

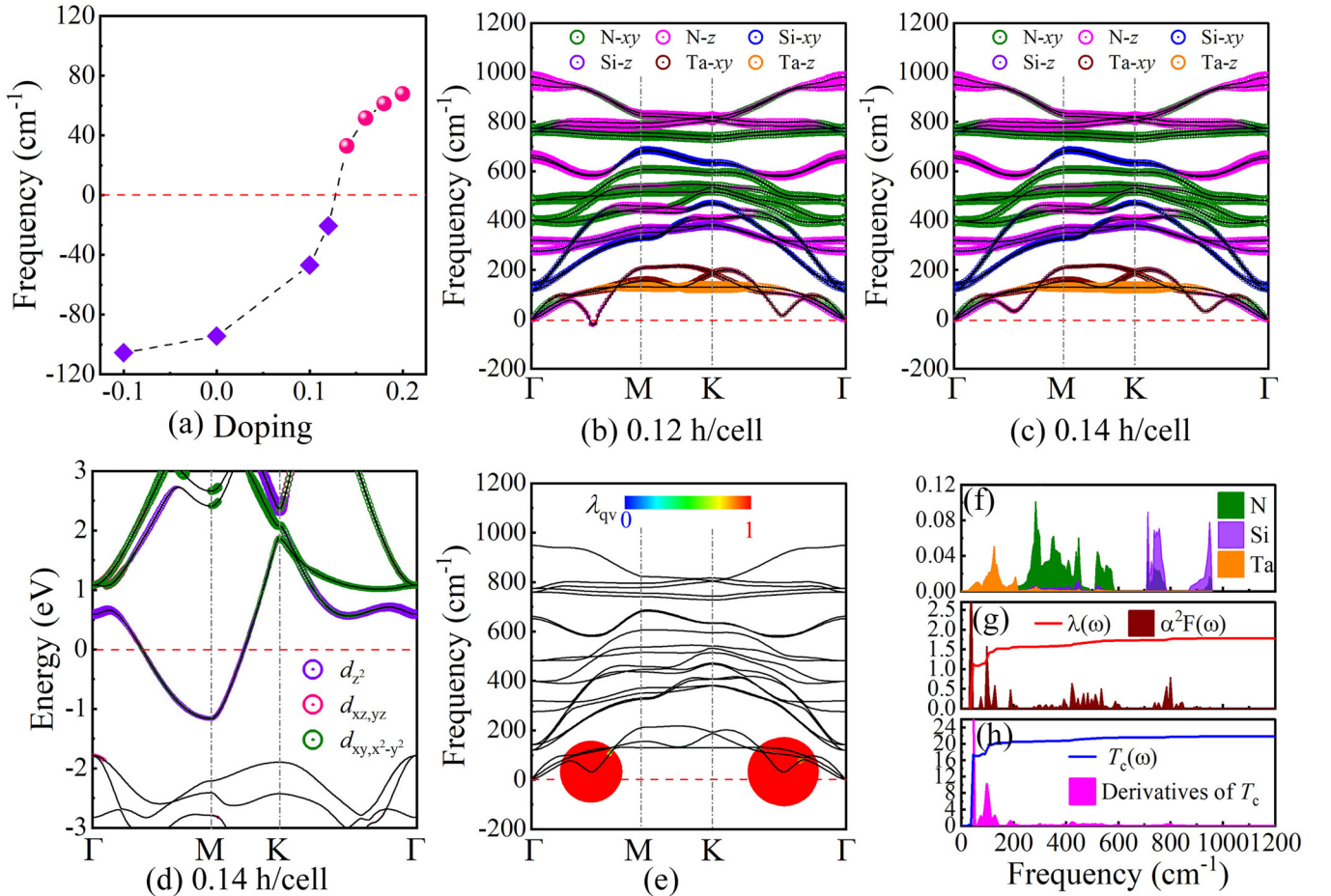


FIG. 4. (a) Variations of the frequency of **a** point in Fig. 1(c) along with the carrier doping. Two typical phonon spectra doped at (b) 0.12 h/cell and (c) 0.14 h/cell. When doped at 0.14 h/cell, the protected band structure for SL 1T-TaSi₂N₄, weighted by the Ti- d_{z^2} , $d_{xz,yz}$ and d_{xy,x^2-y^2} orbitals, is shown in (d). The phonon spectrum for 1T-TaSi₂N₄ monolayer upon doped 0.14 h/cell, weighted by the EPC λ_{qv} . (f) The projected phonon density of states (PhDOS), (g) Eliashberg spectral function $\alpha^2F(\omega)$ as well as its cumulative frequency dependent EPC function $\lambda(\omega)$, and (h) frequency dependent function $T_c(\omega)$ with its derivatives for doped SL 1T-TaSi₂N₄ at 0.14 h/cell.

in Fig. 2(f), the in-plane MSDs of Ta and N from the MD trajectory at 500 K are larger than the other MSD components, indicating the soft mode is mainly induced by the weak Ta-N bonds, consistent with our bond analysis and the vibrational modes shown in Fig. 1(d). Moreover, the in-plane MSD of Ta atoms is greatly larger than that of N atoms, even though Ta atom is much heavier than N. This further demonstrates the major contribution of Ta displacements to the anharmonicity. Apart from the mode at \mathbf{a} point, anharmonic and thermal effects also mainly refine some other out-of-plane modes, including the soft ZA mode as well as modes 8, 9, 14, 15, 20, and 21 in Fig. S3 [39].

To investigate the origin of the CDW orders in SL 1T-TaSi₂N₄, we can study it in following three common scenarios: excitonic insulator, FS nesting, and EPC. Firstly, as shown in Fig. 1(e), SL 1T-TaSi₂N₄ is a robust metal with one band crossing the Fermi level from -1.6 eV to 1.5 eV. So that the excitonic effect cannot turn SL 1T-TaSi₂N₄ to an excitonic insulator [13]. Thus, the excitonic insulator as the potential mechanism in the formation of CDW is denied. In 1973, Chan and Heine derived the criterion for a stable CDW phase with a modulation wave vector \mathbf{q} as follows:

$$\frac{4\eta_{\mathbf{q}}^2}{\hbar\omega_{\text{bare}}} \geq \frac{1}{\chi_{\mathbf{q}}} + (2U_{\mathbf{q}} - V_{\mathbf{q}}), \quad (1)$$

in which $\eta_{\mathbf{q}}$ indicates the EPC matrix element related to a mode at an unrenormalized energy of ω_{bare} , $\chi_{\mathbf{q}}$ is the dielectric response of the conduction electrons, and $U_{\mathbf{q}}$ and $V_{\mathbf{q}}$ are their Coulomb and exchange interactions, respectively [52]. It is clear that the static CDW orders depend on the electron susceptibility $\chi_{\mathbf{q}}$ and EPC. FS nesting, which is always responsible for the origin of CDW, originated from the Peierls idea of electronic instabilities. Besides, the FS nesting can be evaluated quantitatively by calculating the electron susceptibility [53]. The real and imaginary part of susceptibility are defined as

$$\chi'(\mathbf{q}) = \sum_{\mathbf{k}} \frac{f(\varepsilon_{\mathbf{k}}) - f(\varepsilon_{\mathbf{k}+\mathbf{q}})}{\varepsilon_{\mathbf{k}} - \varepsilon_{\mathbf{k}+\mathbf{q}}} \quad (2)$$

and

$$\lim_{\omega \rightarrow 0} \chi''(\mathbf{q}, \omega)/\omega = \sum_{\mathbf{k}} \delta(\varepsilon_{\mathbf{k}} - \varepsilon_F) \delta(\varepsilon_{\mathbf{k}+\mathbf{q}} - \varepsilon_F), \quad (3)$$

respectively, where ε is the energy of electron and f is the Fermi-Dirac distribution function. The FS nesting is the low-frequency limit of the imaginary part of the electron susceptibility in the constant matrix element approximation, which can be easily measured experimentally by neutron scattering. Accordingly, the CDW wave vector must be the peak wave vector. While the stability of an electronic system is determined by the real part of the electron susceptibility, and the nested peak must transfer to the real part of the susceptibility at the same wave vector. In general, both the real part and imaginary part of the electron susceptibility function should have same location at the CDW wave vector, once the FS nesting is the origin of the CDW in a system [12,53]. As depicted in Fig. 3(a), the peaks in the real part of the electron susceptibility locate along the Γ -M path. However, the strongest peak

in the imaginary part of the electron susceptibility occurs at the K points [Fig. 3(b)]. Obviously, the peaks of the real and imaginary parts of the electron susceptibility function exist at different locations, indicating that the FS nesting is not the driving force for the formation of CDW in SL 1T-TaSi₂N₄ [53–55]. Finally, the momentum-dependent EPC helps to explicate the phonon mode softening and the CDW origin, which are strongly associated with the phonon linewidth γ [Eq. (2) in SM] [12,56]. The phonon linewidth γ of the ZA mode is plotted in Fig. 3(c). Clearly, the two highest peaks locate along the Γ -M and K- Γ paths, which are in line with the locations of the two Kohn anomalies in the phonon dispersions. Therefore, the identical positions for the EPC peaks and the Kohn anomalies confirm that the origin of CDW in SL 1T-TaSi₂N₄ is from the momentum-dependent EPC [12].

D. Carrier doping effect on CDW and superconductivity

Electron or hole doping is usually applied to manipulate the CDW [17,57], which can be easily achieved in experiments by using available gating techniques. In this regard, carrier doping effects within the jellium model are further studied for SL 1T-TaSi₂N₄. The variation of the imaginary frequencies at the \mathbf{a} point upon carrier doping is shown in Fig. 4(a). We can see that the electron doping stimulates the CDW orders, while the hole doping can suppress the CDW orders. Increasing the hole concentration, the negative ZA mode lifts up and eventually becomes a positive mode at about 0.14 h/cell [Figs. 4(b) and 4(c)]. Thus, the CDW is completely suppressed at 0.14 h/cell doping, and SL 1T-TaSi₂N₄ turns to be a stable phase. As shown Fig. 4(d), SL 1T-TaSi₂N₄ at 0.14 h/cell doping maintains the main features of the electronic band structure dispersions as its pristine phase. Hole doping only downgrades the Fermi level to some extent. The metallic nature is still mainly contributed by the Ta- d_{z^2} orbitals.

Since the structure under 0.14 h/cell doping is dynamically stable and also exhibits metallic feature, we subsequently study its potential superconductivity within BCS theory. As indicated by the branch magnitude of the EPC λ_{qv} in Fig. 4(e), there are two large EPC values at the two soft-mode points in ZA branch. Meanwhile, as exhibited in Fig. 4(g), the Eliashberg spectral function $a^2F(\omega)$ shows two significant peaks at 44 and 96 cm^{-2} , resulting in a rapid increase of the cumulative $\lambda(\omega)$ and contributing about 79.8% of the total EPC ($\lambda = 1.78$). As a consequence, the superconductivity transition temperature function $T_c(\omega)$ also show two significant peaks simultaneously [Fig. 4(h)]. Based on the full Allen-Dynes formula [Eq. (6) in SM] [39], the T_c of SL 1T-TaSi₂N₄ at 0.14 h/cell doping is estimated to be ~ 21.84 K, which is greatly higher than that of SL 2H-TaN₂ (0.86 K) [29], and comparable to SL 2H-TaSi₂N₄ (24.62 K) [29]. Similar to SL 2H-TaSi₂N₄, the main contribution to the EPC also originates from the low-frequency region, where the in-plane vibrations of Ta atoms (Ta-xy) and out-of-plane vibrations of N atoms (N-z) play the crucial roles [Figs. 4(c) and 4(f)]. Physically, the origin of the superconductivity in SL 1T-TaSi₂N₄ is the coupling between electrons of Ta- d_{z^2} orbitals and phonon from Ta-xy as well as N-z vibrations.

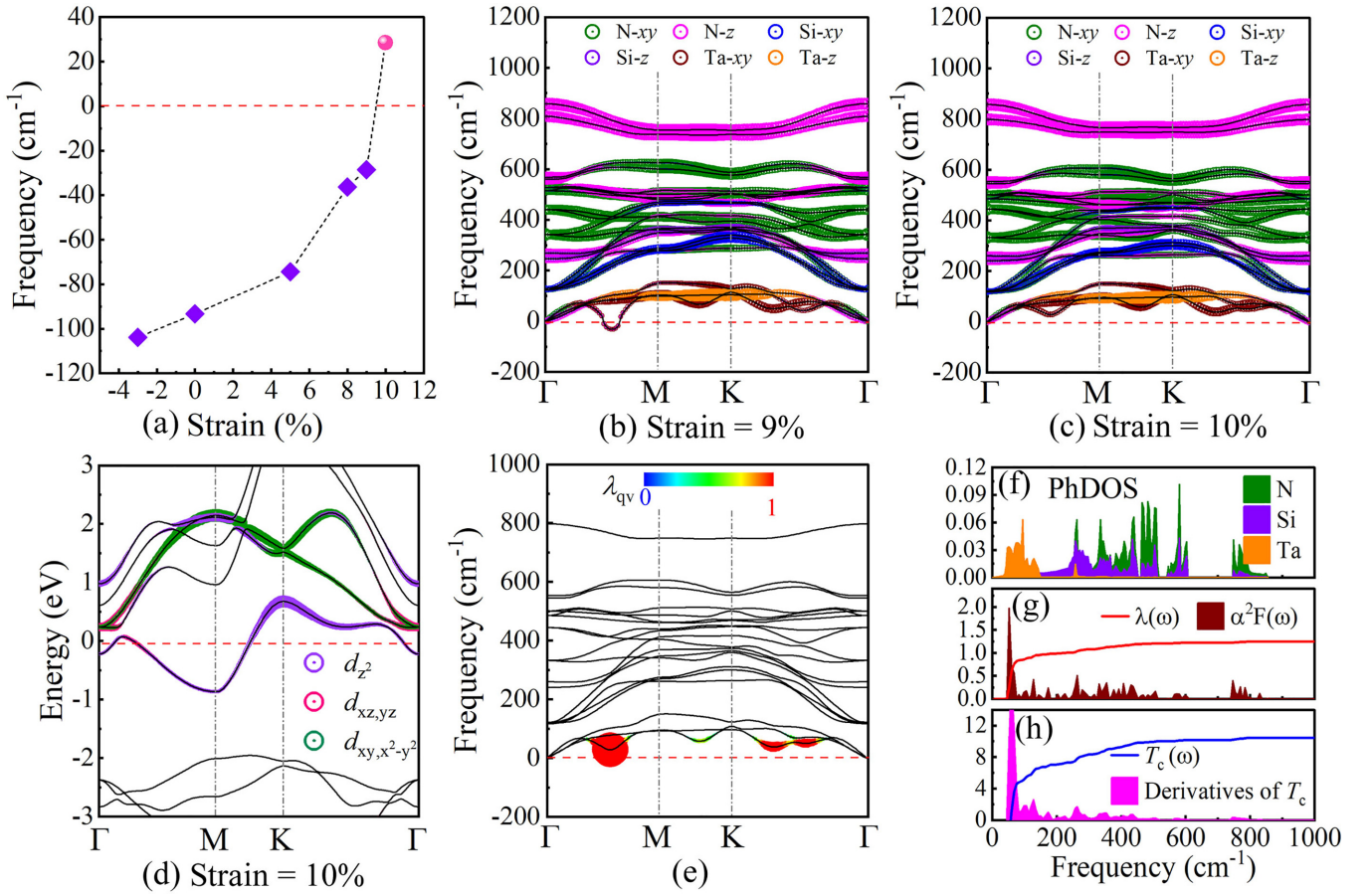


FIG. 5. (a) Changes of the frequency of a point in Fig. 1(c) along with the applied strains. The phonon spectra subjected to the strain of (b) 9% and (c) 10%. (d) Pband for SL 1T-TaSi₂N₄ under the strain of 10%, weighted by the Ti- d_{z^2} , $d_{xz,yz}$ and d_{xy,x^2-y^2} orbitals. (e) The weighted EPC λ_{qv} in the phonon spectrum at the strain of 10%. PhDOS, $\alpha^2F(\omega)$ as well $\lambda(\omega)$, and $T_c(\omega)$ with its derivatives are depicted in (f), (g), and (h), respectively.

E. Strain effect for CDW and superconductivity

Since SL 1T-TaSi₂N₄ is inclined to be obtained by the chemical vapor deposition growth method as MoSi₂N₄ monolayer [21], thus, the external strain effects arising from substrate interactions are addressed here. The evolution of the frequency at the **a** point under the biaxial strain for SL 1T-TaSi₂N₄ is shown in Fig. 5(a). Increasing the compressive strains, the imaginary frequency at the **a** point gradually tends to be positive, and the CDW orders are fully suppressed under the strain of 10% [Figs. 5(b) and 5(c)]. Under this critical strain, SL 1T-TaSi₂N₄ not only shows metallic properties with many band crossing points at the Fermi level [Fig. 5(d)], but also shows possible superconductivity with large EPC λ_{qv} on the soft ZA mode [Fig. 5(e)], similar to the aforementioned doped case. As shown in Fig. 5(g), a major peak of the Eliashberg spectral function $\alpha^2F(\omega)$ at 53 cm⁻² leads to a great enhancement of the $\lambda(\omega)$, contributing about 77.3% to the total λ ($\lambda = 1.09$). Meanwhile, the $T_c(\omega)$ and its derivatives are also in accordance with these results [Fig. 5(h)]. Therefore, the superconductivity of SL 1T-TaSi₂N₄ under the strain of 10% also mainly originates from the coupling of electrons from the Ta- d_{z^2} orbitals and phonon from the Ta-xy and N-z modes in the ZA branch. Finally, its T_c is calculated to be 10.47 K, which is only about half of that in the doped one at 0.14 h/cell. As clearly shown in Fig. 5(e), relatively small

value of T_c is due to the external strain hardens the ZA modes, and thus giving a relatively weak EPC at the soft-mode points, especially for the points along the K- Γ path. Nonetheless, its T_c is higher than that in nitrides superconductor determined by experiments, such as NbN films (6.7 K) [47], TaN thin films (6–8 K) [58], and Nb₂N films (< 1 K) [59].

In the following, we investigate doping effects on SL 1T-TaSi₂N₄ strained at the strain of 10%. For each doping concentration, only the atomic positions are relaxed to ensure that the CDW orders is fully suppressed under the strain of 10%. Since the electron doping leads the strained 1T-TaSi₂N₄ ML to unstable state with some imaginary frequencies (not shown here), thereby, only the relevant superconductive parameters upon hole doping are exhibited in Fig. 6. As expected, the $N(E_F)$ decreases with the increasing of the hole doping concentration, resembling that of ω_{log} . Whereas, the EPC λ is enhanced to 1.54 at 0.3 h/cell doping, and thus the T_c is increased to 15.01 K. Generally speaking, a smaller carrier density near the Fermi level will lead to a lower T_c of the conventional BCS superconductor [60]. On contrast to this ruler, in our case, the inverse behavior is due to that the low frequencies are softened after doping, particularly along the K- Γ path, leading to a higher EPC and T_c (see Fig. S5 in SM) [39]. Although the carrier doping cannot enhance the T_c of this strained one to a large

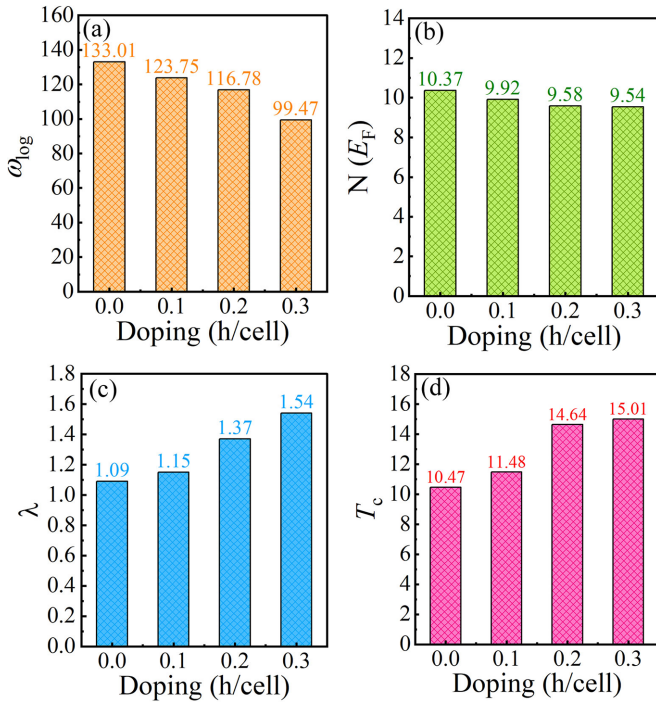


FIG. 6. Variations of four general superconducting parameters: (a) logarithmic average frequency ω_{\log} , (b) the density of states at the Fermi level [$N(E_F)$], (c) EPC constant λ and (d) T_c , when the hole doping is added to SL 1T-TaSi₂N₄ strained at the strain of 10%.

extent, our result could provide clues for future experimental determinations.

Given that 2H-NbSi₂N₄ ML is also a good superconductor with a T_c of 30.4 K [29], here, the 1T phase of NbSi₂N₄ are also studied. Similar to SL 1T-TaSi₂N₄, there are also two Kohn anomalies located along the Γ -M and K- Γ paths with evident imaginary frequencies. In particular, these imaginary modes can also be raised up along with the increase of σ , and then become positive when $\sigma = 0.013$ Ry (see SM Fig. S6) [39]. This critical σ is the same as SL 1T-TaSi₂N₄, approximately meaning similar T_{CDW} for them. However, the CDW orders in 1T-NbSi₂N₄ ML cannot be validly manipulated via the external strains. Although the strain can suppress the CDW orders to some extent, new imaginary modes appear along the

M-K path (see SM Fig. S7) [39]. Therefore, the CDW orders in SL 1T-NbSi₂N₄ cannot be manipulated solely by strain.

IV. CONCLUSION

In conclusion, we have proposed a CDW material candidate, SL 1T-TaSi₂N₄, through first-principle calculations. Similar to some classic CDW materials, the CDW behaviors in SL 1T-TaSi₂N₄ can be simulated by electron temperature, and can be fully suppressed at a Fermi-Dirac smearing width of 0.013 Ry. After including anharmonicity, by performing AIMD calculations, the T_{CDW} is estimated to be around 450–500 K. The large imaginary frequencies of the two Kohn anomalies in ZA modes can be effectively suppressed by finite temperature. Other than the effects of excitonic insulator and FS nesting, it is the EPC that drives the formation of the CDW in this system. Its metallic feature is mainly contributed by the Ta- d_{z^2} orbitals. Intriguingly, both carrier doping and strain can effectively manipulate its CDW orders and can induce superconductivity after eventually suppressing the CDW. When doping at the 0.14 h/cell, a T_c of ~ 21.84 K is predicted. In the case of strain, the T_c is ~ 10.47 K under compression strain of 10%, and it can be further improved to 15.01 K with the help of 0.3 h/cell doping. According to our calculations, the superconductivity is mainly contributed by the coupling between the electrons from Ta- d_{z^2} orbitals and phonons in the soft ZA mode, which is dominated by the Ta- xy and N- z vibrations. Our work provides a promising candidate for studying CDW, superconductivity, and their interplay, thereby giving realistic opportunity for the realization of exotic macroscopic quantum phenomena.

ACKNOWLEDGMENTS

B.-T.W. acknowledges financial support from the Natural Science Foundation of China (Grants No. 12074381 and No. U2330104). L.Z. acknowledges the Natural Science Foundation of China (Grant No. 12374057), the Startup funds of Outstanding Talents of Electronic Science and Technology of China (No. A1098531023 601205), the National Youth Talents Plan of China (No. G05QNQR049). J.G.S. is grateful for the financial support from the Natural Science Foundation of China (Grant No. 12304095).

- [1] E. Morosan, H. W. Zandbergen, B. Dennis, J. Bos, Y. Onose, T. Klimczuk, A. Ramirez, N. Ong, and R. J. Cava, Superconductivity in Cu_xTiSe₂, *Nat. Phys.* **2**, 544 (2006).
- [2] T. Kiss, T. Yokoya, A. Chainani, S. Shin, T. Hanaguri, M. Nohara, and H. Takagi, Charge-order-maximized momentum-dependent superconductivity, *Nat. Phys.* **3**, 720 (2007).
- [3] H. Cercellier, C. Monney, F. Clerc, C. Battaglia, L. Despont, M. G. Garnier, H. Beck, P. Aebi, L. Patthey, H. Berger, and H. Forro, Evidence for an excitonic insulator phase in 1T-TiSe₂, *Phys. Rev. Lett.* **99**, 146403 (2007).
- [4] M. Eichberger, H. Schäfer, M. Krumova, M. Beyer, J. Demsar, H. Berger, G. Moriena, G. Sciaini, and R. D. Miller, Snapshots

of cooperative atomic motions in the optical suppression of charge density waves, *Nature (London)* **468**, 799 (2010).

- [5] M. Chhowalla, H. S. Shin, G. Eda, L.-J. Li, K. P. Loh, and H. Zhang, The chemistry of two-dimensional layered transition metal dichalcogenide nanosheets, *Nat. Chem.* **5**, 263 (2013).
- [6] X. Xi, L. Zhao, Z. Wang, H. Berger, L. Forró, J. Shan, and K. F. Mak, Strongly enhanced charge-density-wave order in monolayer NbSe₂, *Nat. Nanotechnol.* **10**, 765 (2015).
- [7] P. Chen, Y.-H. Chan, X.-Y. Fang, Y. Zhang, M.-Y. Chou, S.-K. Mo, Z. Hussain, A.-V. Fedorov, and T.-C. Chiang, Charge density wave transition in single-layer titanium diselenide, *Nat. Commun.* **6**, 8943 (2015).

- [8] G. Venditti and S. Caprara, Charge-density waves vs. superconductivity: Some results and future perspectives, *Condens. Matter* **8**, 54 (2023).
- [9] C. Battaglia, H. Cercellier, F. Clerc, L. Despont, M. G. Garnier, C. Koitzsch, P. Aebi, H. Berger, L. Forró, and C. Ambrosch-Draxl, Fermi-surface-induced lattice distortion in NbTe₂, *Phys. Rev. B* **72**, 195114 (2005).
- [10] M. D. Johannes, I. I. Mazin, and C. A. Howells, Fermi-surface nesting and the origin of the charge-density wave in NbSe₂, *Phys. Rev. B* **73**, 205102 (2006).
- [11] J. G. Si, W. J. Lu, H. Y. Wu, H. Y. Lv, X. Liang, Q. J. Li, and Y. P. Sun, Origin of the multiple charge density wave order in 1T-VSe₂, *Phys. Rev. B* **101**, 235405 (2020).
- [12] R. Ku, L. Yan, J.-G. Si, S. Zhu, B.-T. Wang, Y. Wei, K. Pang, W. Li, and L. Zhou, *Ab initio* investigation of charge density wave and superconductivity in two-dimensional Janus 2H/1T-MoSH monolayers, *Phys. Rev. B* **107**, 064508 (2023).
- [13] J. van Wezel, P. Nahai-Williamson, and S. S. Saxena, Exciton-phonon-driven charge density wave in TiSe₂, *Phys. Rev. B* **81**, 165109 (2010).
- [14] A. Kogar, M. S. Rak, S. Vig, A. A. Husain, F. Flicker, Y. I. Joe, L. Venema, G. J. MacDougall, T. C. Chiang, E. Fradkin *et al.*, Signatures of exciton condensation in a transition metal dichalcogenide, *Science* **358**, 1314 (2017).
- [15] B. Sipos, A. F. Kusmartseva, A. Akrap, H. Berger, L. Forró, and E. Tutiš, From Mott state to superconductivity in 1T-TaS₂, *Nat. Mater.* **7**, 960 (2008).
- [16] Y. Yu, F. Yang, X. F. Lu, Y. J. Yan, Y.-H. Cho, L. Ma, X. Niu, S. Kim, Y.-W. Son, D. Feng *et al.*, Gate-tunable phase transitions in thin flakes of 1T-TaS₂, *Nat. Nanotechnol.* **10**, 270 (2015).
- [17] L. J. Li, E. C. T. O'Farrell, K. P. Loh, G. Eda, B. Özyilmaz, and A. H. Castro Neto, Controlling many-body states by the electric-field effect in a two-dimensional material, *Nature (London)* **529**, 185 (2016).
- [18] Y. Zhong, Y. Wang, S. Han, Y.-F. Lv, W.-L. Wang, D. Zhang, H. Ding, Y.-M. Zhang, L. Wang, K. He *et al.*, Nodeless pairing in superconducting copper-oxide monolayer films on Bi₂ST₂CaCu₂O_{8+δ}, *Sci. Bull.* **61**, 1239 (2016).
- [19] A. W. Tsen, R. Hovden, D. Wang, Y. D. Kim, J. Okamoto, K. A. Spoth, Y. Liu, W. Lu, Y. Sun, J. C. Hone *et al.*, Structure and control of charge density waves in two-dimensional 1T-TaS₂, *Proc. Natl. Acad. Sci.* **112**, 15054 (2015).
- [20] M. J. Wei, W. J. Lu, R. Xiao, H. Y. Lv, P. Tong, W. Song, and Y. Sun, Manipulating charge density wave order in monolayer 1T-TiSe₂ by strain and charge doping: A first-principles investigation, *Phys. Rev. B* **96**, 165404 (2017).
- [21] Y.-L. Hong, Z. Liu, L. Wang, T. Zhou, W. Ma, C. Xu, S. Feng, L. Chen, M.-L. Chen, D.-M. Sun *et al.*, Chemical vapor deposition of layered two-dimensional MoSi₂N₄ materials, *Science* **369**, 670 (2020).
- [22] L. Wang, Y. Shi, M. Liu, A. Zhang, Y.-L. Hong, R. Li, Q. Gao, M. Chen, W. Ren, H.-M. Cheng *et al.*, Intercalated architecture of MA₂Z₄ family layered van der Waals materials with emerging topological, magnetic and superconducting properties, *Nat. Commun.* **12**, 2361 (2021).
- [23] L. Yan, A. Huang, B.-T. Wang, J.-G. Si, Y. M. Ding, and L. Zhou, Theoretical prediction of two-dimensional 1T - MSiN₃ (M = V, Nb) with direct bandgap and long carrier lifetime, *Phys. Rev. B* **108**, 155309 (2023).
- [24] Y. Yu, J. Zhou, Z. Guo, and Z. Sun, Novel two-dimensional janus MoSiGeN₄ and WSiGeN₄ as highly efficient photocatalysts for spontaneous overall water splitting, *ACS Appl. Mater. Interfaces* **13**, 28090 (2021).
- [25] C. Xiao, R. Sa, Z. Cui, S. Gao, W. Du, X. Sun, X. Zhang, Q. Li, and Z. Ma, Enhancing the hydrogen evolution reaction by non-precious transition metal (non-metal) atom doping in defective MoSi₂N₄ monolayer, *Appl. Surf. Sci.* **563**, 150388 (2021).
- [26] B. Mortazavi, F. Shojaei, B. Javvaji, T. Rabczuk, and X. Zhuang, Outstandingly high thermal conductivity, elastic modulus, carrier mobility and piezoelectricity in two-dimensional semiconducting CrC₂N₄: A first-principles study, *Mater. Today Energy* **22**, 100839 (2021).
- [27] A. Bafekry, M. Faraji, M. Fadlallah, A. A. Ziabari, A. B. Khatibani, S. Feghhi, M. Ghergherehchi, and D. Gogova, Adsorption of habitat and industry-relevant molecules on the MoSi₂N₄ monolayer, *Appl. Surf. Sci.* **564**, 150326 (2021).
- [28] J.-S. Yang, L. Zhao, L. Shi-Qi, H. Liu, L. Wang, M. Chen, J. Gao, and J. Zhao, Accurate electronic properties and non-linear optical response of two-dimensional MA₂Z₄, *Nanoscale* **13**, 5479 (2021).
- [29] L. Yan, B.-T. Wang, X. Huang, Q. Li, K. Xue, J. Zhang, W. Ren, and L. Zhou, Surface passivation induced a significant enhancement of superconductivity in layered two-dimensional MSi₂N₄ (M = Ta and Nb) materials, *Nanoscale* **13**, 18947 (2021).
- [30] B.-T. Wang, P.-F. Liu, J.-J. Zheng, W. Yin, and F. Wang, First-principles study of superconductivity in the two- and three-dimensional forms of PbTiSe₂: Suppressed charge density wave in 1T-TiTe₂, *Phys. Rev. B* **98**, 014514 (2018).
- [31] P. Giannozzi, S. Baroni, N. Bonini, M. Calandra, R. Car, C. Cavazzoni, D. Ceresoli, G. L. Chiarotti, M. Cococcioni, I. Dabo *et al.*, QUANTUM ESPRESSO: A modular and open-source software project for quantum simulations of materials, *J. Phys.: Condens. Matter* **21**, 395502 (2009).
- [32] P. Giannozzi Jr, O. Andreussi, T. Brumme, O. Bunau, M. B. Nardelli, M. Calandra, R. Car, C. Cavazzoni, D. Ceresoli, M. Cococcioni *et al.*, Advanced capabilities for materials modelling with QUANTUM ESPRESSO, *J. Phys.: Condens. Matter* **29**, 465901 (2017).
- [33] J. P. Perdew, K. Burke, and M. Ernzerhof, Generalized gradient approximation made simple, *Phys. Rev. Lett.* **77**, 3865 (1996).
- [34] D. R. Hamann, Optimized norm-conserving Vanderbilt pseudopotentials, *Phys. Rev. B* **88**, 085117 (2013).
- [35] O. Hellman, I. Abrikosov, and S. Simak, Lattice dynamics of anharmonic solids from first principles, *Phys. Rev. B* **84**, 180301(R) (2011).
- [36] O. Hellman and I. A. Abrikosov, Temperature-dependent effective third-order interatomic force constants from first principles, *Phys. Rev. B* **88**, 144301 (2013).
- [37] F. Eriksson, E. Fransson, and P. Erhart, The hiphive package for the extraction of high-order force constants by machine learning, *Adv. Theory Simul.* **2**, 1800184 (2019).
- [38] J. Bardeen, L. N. Cooper, and J. R. Schrieffer, Theory of superconductivity, *Phys. Rev.* **108**, 1175 (1957).
- [39] See Supplemental Material at <http://link.aps.org/supplemental/10.1103/PhysRevB.109.134502> for detailed methods for calculating superconductivity, ELF plots, AIMD simulations, orientation-dependent $Y(\theta)$ and $\nu(\theta)$, spatial vibration modes,

- convergence of the free energy, Phonon dispersions of 1T-NbSi₂N₄.
- [40] F. Giustino, Electron-phonon interactions from first principles, *Rev. Mod. Phys.* **89**, 015003 (2017).
- [41] W. L. McMillan, Transition temperature of strong-coupled superconductors, *Phys. Rev.* **167**, 331 (1968).
- [42] P.-F. Liu, F. Zheng, J. Li, J.-G. Si, L. Wei, J. Zhang, and B.-T. Wang, Two-gap superconductivity in a Janus MoSH monolayer, *Phys. Rev. B* **105**, 245420 (2022).
- [43] L. Yan, J. Zhu, B.-T. Wang, J. He, H.-Z. Song, W. Chu, S. Tretiak, and L. Zhou, Two-dimensional MOene: From superconductors to direct semiconductors and weyl fermions, *Nano Lett.* **22**, 5592 (2022).
- [44] W. Tang, E. Sanville, and G. Henkelman, A grid-based Bader analysis algorithm without lattice bias, *J. Phys.: Condens. Matter* **21**, 084204 (2009).
- [45] F. Mouhat and F.-X. Coudert, Necessary and sufficient elastic stability conditions in various crystal systems, *Phys. Rev. B* **90**, 224104 (2014).
- [46] B. Song, Y. Zhou, H.-M. Yang, J.-H. Liao, L.-M. Yang, X.-B. Yang, and E. Ganz, Two-dimensional anti-Van't Hoff/Le Bel array AlB₆ with high stability, unique motif, triple dirac cones, and superconductivity, *J. Am. Chem. Soc.* **141**, 3630 (2019).
- [47] Y. Noat, V. Cherkez, C. Brun, T. Cren, C. Carbillet, F. Debontridder, K. Ilin, M. Siegel, A. Semenov, H.-W. Hübers *et al.*, Unconventional superconductivity in ultrathin superconducting nbn films studied by scanning tunneling spectroscopy, *Phys. Rev. B* **88**, 014503 (2013).
- [48] T. Han, S. Y. Wang, B. Han, Y. Liu, F. Li, and L. Wang, Two-dimensional potassium borides with hidden kagome-like lattice: Topological semimetals, van hove singularities, and superconductivity, *Phys. Rev. B* **107**, 235154 (2023).
- [49] J.-A. Yan, M. A. D. Cruz, B. Cook, and K. Varga, Structural, electronic and vibrational properties of few-layer 2H- and 1T-TaSe₂, *Sci. Rep.* **5**, 16646 (2015).
- [50] O. Hellman, P. Steneteg, I. A. Abrikosov, and S. I. Simak, Temperature dependent effective potential method for accurate free energy calculations of solids, *Phys. Rev. B* **87**, 104111 (2013).
- [51] J. S. Zhou, L. Monacelli, R. Bianco, I. Errea, F. Mauri, and M. Calandra, Anharmonicity and doping melt the charge density wave in single-layer TiSe₂, *Nano Lett.* **20**, 4809 (2020).
- [52] S.-K. Chan and V. Heine, Spin density wave and soft phonon mode from nesting fermi surfaces, *J. Phys. F* **3**, 795 (1973).
- [53] M. D. Johannes and I. I. Mazin, Fermi surface nesting and the origin of charge density waves in metals, *Phys. Rev. B* **77**, 165135 (2008).
- [54] K. Zhang, X. Liu, H. Zhang, K. Deng, M. Yan, W. Yao, M. Zheng, E. F. Schwier, K. Shimada, J. D. Denlinger *et al.*, Evidence for a quasi-one-dimensional charge density wave in cte by angle-resolved photoemission spectroscopy, *Phys. Rev. Lett.* **121**, 206402 (2018).
- [55] X. Zhu, Y. Cao, J. Zhang, E. W. Plummer, and J. Guo, Classification of charge density waves based on their nature, *Proc. Natl. Acad. Sci.* **112**, 2367 (2015).
- [56] J.-G. Si, W.-J. Lu, Y.-P. Sun, P.-F. Liu, and B.-T. Wang, Charge density wave and pressure-dependent superconductivity in the kagome metal CsV₃Sb₅: A first-principles study, *Phys. Rev. B* **105**, 024517 (2022).
- [57] I. Vaskivskiy, I. Mihailovic, S. Brazovskii, J. Gospodaric, T. Mertelj, D. Svetin, P. Sutar, and D. Mihailovic, Fast electronic resistance switching involving hidden charge density wave states, *Nat. Commun.* **7**, 11442 (2016).
- [58] S. Chaudhuri, I. J. Maasilta, L. Chandernagor, M. Ging, and M. Lahtinen, Fabrication of superconducting tantalum nitride thin films using infrared pulsed laser deposition, *J. Vac. Sci. Technol. A* **31**, 061502 (2013).
- [59] B. Gajar, S. Yadav, D. Sawle, K. K. Maurya, A. Gupta, R. Aloysius, and S. Sahoo, Substrate mediated nitridation of niobium into superconducting Nb₂N thin films for phase slip study, *Sci. Rep.* **9**, 8811 (2019).
- [60] J. Wang, Superconductivity in topological semimetals, *Nat. Sci. Rev.* **6**, 199 (2019).